Computational aeroacoustics to identify sound sources in the generation of sibilant /s/

Arnau Pont*

Centre Internacional de Mètodes Numèrics en Enginyeria,

Universitat Politècnica de Catalunya,

C/ Gran Capità, s/n, Campus Nord UPC,

Barcelona, E-08034, Catalonia, Spain.

Oriol Guasch

GTM Grup de recerca en Tecnologies Mèdia, La Salle, Universitat Ramon Llull,

C/Quatre Camins 30, Barcelona, E-08022, Catalonia, Spain

Joan Baiges and Ramon Codina

Universitat Politècnica de Catalunya,

C/ Jordi Girona 1-3, Edifici C1, Campus Nord UPC,

Barcelona, E-08034, Catalonia, Spain.

Annemie Van Hirtum

GIPSA-Lab, UMR CNRS 5216, Grenoble Alpes Univ.,

Grenoble Campus, St Martin d'Heres, F-38402, France

(Dated: May 18, 2017)

Abstract

A sibilant fricative /s/ is generated when the turbulent jet in the narrow channel between the tongue blade and the hard palate is deflected downwards through the incisors' gap, and impinges the inter-space between the lower incisors and the lower lips. The flow eddies in that region become a source of direct aerodynamic sound, which is also diffracted by the upper incisors and radiated outwards. The numerical simulation of this phenomena is complex. The spectrum of an /s/ typically peaks between $4-10$ kHz, which implies using very fine computational meshes to capture the eddies producing such high frequencies. In this work, a large-scale computation of the aeroacoustics of /s/ has been performed for a realistic vocal tract geometry, resorting to two different acoustic analogies. A stabilized finite element method that acts as a large eddy simulation model has been adopted to solve the flow dynamics. Also, a numerical strategy has been implemented which allows determining, in a single computational run, the separate contributions from the direct turbulent sound and the sound diffracted by the upper incisors, to the radiated sibilant /s/. Results are presented for points located close to the mouth exit showing the relative influence of the sources of sound depending on frequency.

_____

* apont@cimne.upc.edu

I. INTRODUCTION

In this work, we aim at better understanding the generation and radiation mechanisms of sibilant /s/, by means of computational aeroacoustics (CAA) performed on a realistic vocal tract geometry. In particular, we are interested in determining the separate acoustic contributions to points near the mouth exit from the flow noise generated in that region, and from its diffraction by the upper incisors.

The sibilant fricative /s/ is produced when the turbulent jet leaving the glottis is accelerated in the constriction between the tongue blade and the hard palate, passes through the incisors' gap, and impinges the cavity between the lower incisors and the lower lips. This results in the generation of aerodynamic noise, which in turn gets diffracted by the incisors and radiated outwards. The emitted sound has a wide-band spectral content that typically peaks between 4-10 kHz, as observed on human speakers [see e.g., 1–3]. Though the articulators are constantly in movement during speech [see e.g., 4], stationary vocal tract walls are always assumed when modeling a sustained fricative sound for simplicity.

A detailed analytical model to describe the production of /s/ was proposed in [5]. In that model, the diffraction of the sound generated by the turbulent boundary layer (TBL) attached to the incisors was considered as the main noise contributor. A compact Green function that accounted for a simplified geometry of the incisors and the vocal tract was deduced and convolved with a theoretical model for the wall pressure wavenumber-frequency spectrum [see e.g., 6], to predict the acoustic pressure at the far-field. More recently, [7] presented large eddy simulations (LES) on a 3D realization of the geometry in [5]. They reported that it is actually at the cavity between the lower incisors and the lower lips where most of the aeroacoustic source terms concentrate. The simulations in the present work with a realistic vocal tract support that conclusion. In addition, they will essentially show that for points in the vicinity of the mouth, the direct aerodynamic sound contribution from the eddies within the lower incisors-lips cavity dominate the acoustic spectrum at low frequencies, whereas diffraction by the upper incisors governs the high frequency range of the spectrum.

To validate these assertions, the numerical strategy in [8] has been implemented. We note that in most hybrid approaches to CAA a two step procedure is followed [see e.g., 9]. First, an LES computation is carried out by means of a finite element (FEM) (or a finite volume)

approach, to obtain the aerodynamic noise source terms. These terms are secondly input in an acoustic analogy that is solved resorting to an integral formulation [see e.g., 10, 11], which becomes discretized by a boundary element method (BEM). Yet, the proposal in [8] relies on different grounds. The method only makes use of a single FEM code that allows one to solve, in a single computational run, an LES for the incompressible Navier-Stokes equations, a first wave equation for the direct flow noise contribution, and a second wave equation for the sound diffracted by the incisors. This procedure circumvents an inconsistency related to the numerical solution of Curle's dipolar integral term for low Mach numbers [11], given that the total pressure to be input in that integral cannot be obtained from an incompressible LES simulation [see e.g. 8, 12].

In this work, the focus will be placed on the acoustic results of the above strategy rather than on the LES ones, which will be only described qualitatively, together with the implemented FEM strategy. It is to be noted that 3D LES simulations of flow passing around teeth-shaped obstacles to better understand the underlying physics of /s/ where already reported in [13, 14] and in [15]. Simulations of flow passing through simplified geometries with constrictions of different sizes have also been conducted [16]. [17] also resorted to LES to analyze the flow dynamics of /s/ in a realistic vocal tract geometry. As said before, more recently, [7] presented simulations on a 3D realization of the geometry in [5]. On the other hand, the LES in this work has been solved with the stabilized FEM method in [18], which behaves as an implicit LES model [see e.g., 19, 20]. In implicit LES methods, the additional terms included in the equations to avoid numerical instabilities simultaneously act as turbulence models. These have been proven numerically on well-known benchmark turbulent tests for the strategy in [18], [see e.g., 21–23], as well as through analytical reasoning [see 24].

As regards the acoustic formulations to get the contributions from the direct flow noise in the lower incisors-lips cavity, and from the incisors diffraction, one should ideally resort to approaches that could account for the unsteady flow in the vocal tract. The most relevant ones for that purpose are probably the linearized Euler equations [see e.g., 25], or some of its source filtered counterparts to leave aside the vorticity and entropy modes, like the acoustic perturbation equations [APE, see 26]. In [27], a low Mach number for the APE was introduced (see [28] for a full numerical solution retaining all terms). In the case of very low Mach number flows, like those encountered in voice production, the APE in [27] can be

further simplified to the acoustic analogy in [29]. The wave operator in this analogy is just the standard wave equation, like in Lighthill's analogy [30], yet the double time derivative of the incompressible pressure field is used as the source term, instead of the double divergence of the Reynolds tensor of the incompressible velocity field. It can be shown that this allows the filtering of some pseudosound at the flow region (the term pseudosound refers to pressure fluctuations indistinguishable by a single microphone from proper sound, see, e.g., [31]). In this piece of research both, Lighthill's and the analogy in [29] will be employed.

To end this introductory section, we would like to remark that aside from static vowel sounds, for which a large amount of literature is available [see e.g., 32–41], few works can be found in literature addressing the numerical simulation of other speech sounds. The reason for that is probably the complex physics beneath their generation and the associated high computational cost. An exception that has received some recent attention is that of vowel-vowel utterances in [42]. Also, attention has been paid to some unvoiced sounds (see e.g., [43]) and in particular to fricative sounds. Related to the present work, we shall cite [44] where different computational fluid dynamics (CFD) formulations were tested for fricative /ʃ/, using realistic two (2D) and three (3D) dimensional vocal tract geometries. That study compared the performance of a compressible CFD simulation, an incompressible LES and a Reynolds averaged Navier-Stokes (RANS) approach. Though a rather coarse mesh was used, the study arrived at some interesting conclusions. As expected, the RANS simulation provided no reliable results but the compressible CFD and incompressible LES combined with an acoustic analogy yielded proper outputs. Another interesting and unexpected result was that although the flow field from 2D simulations did not match at all with the 3D one, that was not the case for the 2D acoustic pressure field, which was quite similar to the 3D one.

This paper is organized as follows. The methodology that has been followed to perform the simulations is detailed in Sec. II. The later includes a description of the realistic vocal tract geometry for sibilant /s/, the formulation of the acoustic analogies and the splitting strategy between turbulent and diffracted sound that has been implemented. It also outlines the numerical strategy used to solve the involved partial differential equations and includes specific details on how the numerical simulations have been run. The results of the latter are presented in Sec. III, with special emphasis on the characteristics of the generated aerodynamic sound. Conclusions close the paper in Sec. IV.
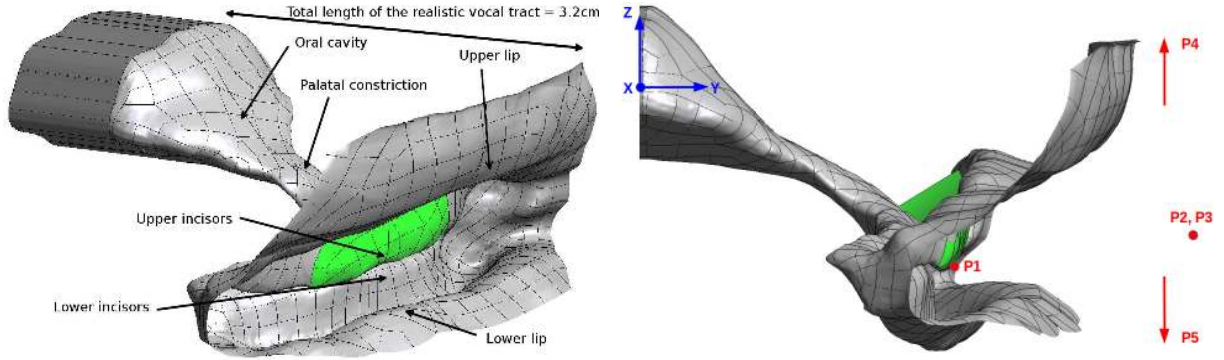
FIG. 1. 3D realistic vocal tract geometry for /s/ with upper incisors highlighted in green. Measuring points P4 and P5 are placed at the far-field. (Color online)

II. METHODOLOGY

A. Vocal tract model

The vocal tract geometry used for the simulations was obtained from a cone-beam CT scan (CB MercuRay, 512 slices of 512 pixel × 512 pixel grid with accuracy ±0.1 mm) in [45] and [46], from which a physical replica was constructed. The geometry (see Fig. 1) corresponds to an adult male Japanese native speaker with normal dentition (angle Class I) without any speech disorder, in normal sitting position. The subject was instructed to sustain phoneme [s] at a medium loudness (with a flow rate ∼ 21 l/min) during 10 s. The entire vocal tract was imaged, but only the characteristic fricative portion (∼ 32 mm) was reconstructed for the replica.

As observed in Fig. 1, it is not necessary to model the whole vocal tract from glottis to lips to produce sibilant /s/, but just the portion where the generating mechanisms take place like in [5]. This includes the constricted passage between the tongue blade and the hard palate (the section with minimum area has a hydraulic diameter of 2.1 mm), the lower and upper incisors (highlighted in green in the figure) and the lips. According to [45], the initial flow conditions upstream (geometry and Reynolds number) do have an influence on the modulation of the acoustic spectrum of fricatives, but do not play an essential role in the physiological mechanisms that lead to the generation of this phoneme. Since the further characterization of the sound [s] depending on gender, age or sex is not part of this work, these factors have not been taken into account.

6

B. Problem formulation

1. Acoustic analogies

As said in the Introduction, in this work use will be made of the celebrated Lighthill acoustic analogy [see 30] and of the analogy in [29]. For low Mach numbers, Lighthill's tensor can be well approximated by the double divergence of the Reynolds tensor of the incompressible velocity field. If one considers a computational domain Ω_v with outer boundary Γ_∞, and a rigid body embedded in it with boundary Γ_w and external normal $\boldsymbol{n}$, the Lighthill acoustic analogy problem reads (see Fig. 2),

$$\frac{1}{c_0^2}\frac{\partial^2 p}{\partial t^2} - \nabla^2 p = \rho_0\left(\nabla \otimes \nabla\right) : \left(\boldsymbol{u}^0 \otimes \boldsymbol{u}^0\right) \text{ in } \Omega_v, \tag{1a}$$

$$\frac{\partial p}{\partial \boldsymbol{n}} = -\frac{1}{c_0}\frac{\partial p}{\partial t} \text{ on } \Gamma_\infty, \ t > 0, \tag{1b}$$

$$\frac{\partial p}{\partial \boldsymbol{n}} = 0 \text{ on } \Gamma_w, \ t > 0, \tag{1c}$$

$$p = 0, \ \frac{\partial p}{\partial t} = 0 \text{ in } \Omega_v, \ t = 0. \tag{1d}$$

In Eq. (1), $p(\boldsymbol{x}, t)$ stands for the acoustic pressure fluctuations and $\boldsymbol{u}^0(\boldsymbol{x}, t)$ for the incompressible velocity field obtained e.g., from a CFD computation. ρ_0 stands for the flow density and c_0 for the speed of sound. In the second line, (1b) introduces a Sommerfeld non-reflecting condition on Γ_∞ and in the third one, (1c) expresses a rigid wall assumption for the immersed body. The initial conditions are set in (1d). The source term $\rho_0\left(\nabla \otimes \nabla\right) : \left(\boldsymbol{u}^0 \otimes \boldsymbol{u}^0\right)$ in Eq. (1) is often rewritten as $\rho_0\left(\nabla \otimes \boldsymbol{u}^0\right) : \left(\nabla \otimes \boldsymbol{u}^0\right)^\top$ for computations ($\top$ denotes transpose), given that $\nabla \cdot \boldsymbol{u}^0 = 0$ (see e.g., [47]).

With regard to the acoustic analogy in [29], it can be obtained from the low Mach APE equations in [27], by simply neglecting the mean velocity field and combining the momentum and continuity equations to get the scalar wave equation for the acoustic pressure. Alternatively, the analogy was originally derived from the following straightforward reasoning. Taking the divergence of the Navier-Stokes momentum conservation equation results in the Poisson equation $\nabla^2 p^0 = -\rho_0\left(\nabla \otimes \nabla\right) : \left(\boldsymbol{u}^0 \otimes \boldsymbol{u}^0\right)$, which allows one to replace Eq. (1a)

with

$$\frac{1}{c_0^2}\frac{\partial^2 p}{\partial t^2} - \nabla^2 p = -\nabla^2 p^0. \tag{2}$$

This equation is interesting for the following reason. It is well known that the acoustic pressure predicted by Lighthill's analogy is only valid far away from the source region, where no flow motion occurs. If one needs to determine the acoustic pressure field close to the generation area it becomes necessary to filter out the *pseudosound* due to non-acoustic pressure fluctuations. In the case of a flow with very small mean convection velocity, [29] proposed to do so by splitting the pressure into its incompressible *pseudosound*, $p^0(\boldsymbol{x}, t)$, and acoustic, $p^a(\boldsymbol{x}, t)$, components, i.e., $p(\boldsymbol{x}, t) = p^0(\boldsymbol{x}, t) + p^a(\boldsymbol{x}, t)$. Inserting this factorization in Eq. (2) results in the following wave equation for the acoustic pressure fluctuations

$$\frac{1}{c_0^2}\frac{\partial^2 p^a}{\partial t^2} - \nabla^2 p^a = -\frac{1}{c_0^2}\frac{\partial^2 p^0}{\partial t^2}, \tag{3}$$

which is to be supplemented with the boundary and initial conditions (1b)-(1d), now for $p^a(\boldsymbol{x}, t)$.

2. Quadrupole and dipole contributions to the acoustic pressure

To determine the contributions to the utterance of [s] from the quadrupole noise generated by the turbulent jet exiting the mouth, and from the dipole noise due to the acoustic pressure diffraction by the upper incisors, one could typically resort, as said before, to Curle's formulation [see 11]. However, in the case of low Mach number flows a severe difficulty appears when trying to account for the rigid body (e.g., the incisors) contribution to the far field. The reason is that the surface integral in Curle's formulation involves the total pressure, which includes both the incompressible and acoustic fluctuations. Obviously, the later cannot be obtained from an incompressible CFD simulation.

Though recently some proposals have been made to at least partially mitigate that problem in the framework of integral formulations [see e.g. 12], in [8], a very different approach was suggested. The approach considers that the acoustic dipole distribution of Curle's surface integral corresponds, in fact, to the diffraction of the turbulent noise generated by the jet flow [see e.g., 48]. On the one hand, the proposed methodology circumvents the total pressure difficulty in Curle's surface term. On the second hand, it avoids the need to resort
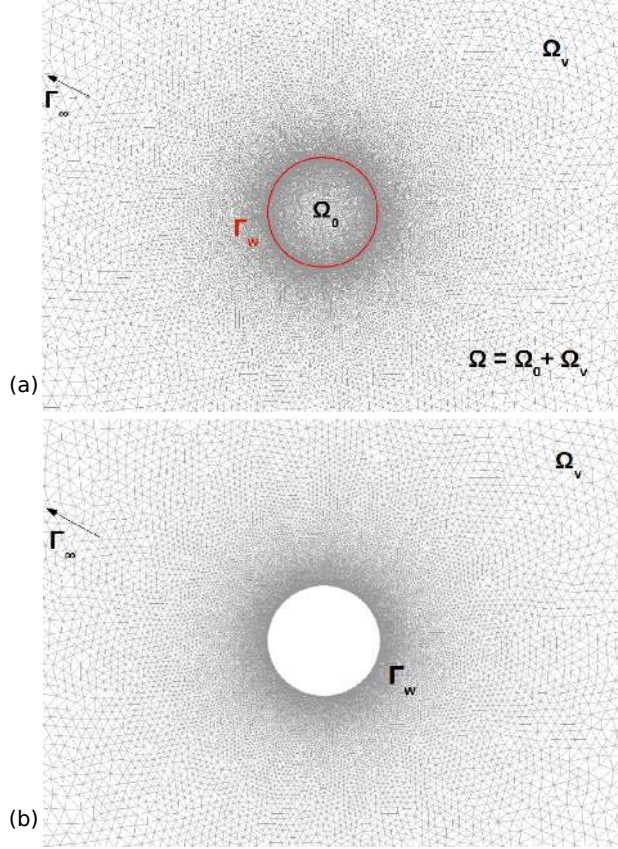
FIG. 2. Domains for computing (a) the incident acoustic pressure and (b) the diffracted acoustic pressure in the proposed splitting strategy for aeroacoustics. (Color online)

to integral formulations, and one can obtain the flow field in the vocal tract, the noise generated by the jet flow at the mouth exit, and the noise contribution from the incisors in a single computational run.

The cornerstone of the method consists in splitting the acoustic pressure, $p(\boldsymbol{x}, t)$ in Eq. (1) (the same holds for $p^a(\boldsymbol{x}, t)$ in Eq. (3)), into incident and diffracted components $p(\boldsymbol{x}, t) = p_i(\boldsymbol{x}, t) + p_d(\boldsymbol{x}, t)$. This leaves one with two wave equations, one for $p_i(\boldsymbol{x}, t)$ and the other one for $p_d(\boldsymbol{x}, t)$, which are solved subsequently in slightly different domains (see Fig. 2). The procedure goes as follows. Once an acoustic source term $s(\boldsymbol{x}, t)$ is obtained from an incompressible CFD computation, for instance,

$$s(\boldsymbol{x}, t) = \begin{cases} \rho_0 \left(\nabla \otimes \nabla \right) : \left(\boldsymbol{u}^0 \otimes \boldsymbol{u}^0 \right) \\ -c_0^{-2} \, \partial^2 p^0 / \partial t^2, \end{cases} \tag{4}$$

9

$s(\boldsymbol{x}, t)$ is used as the inhomogeneous term in the wave equation for the incident pressure component,

$$\frac{1}{c_0^2} \frac{\partial^2 p_i}{\partial t^2} - \nabla^2 p_i = s \text{ in } \Omega \tag{5a}$$

$$\frac{\partial p_i}{\partial \boldsymbol{n}} = -\frac{1}{c_0} \frac{\partial p_i}{\partial t} \text{ on } \Gamma_\infty, \ t > 0 \tag{5b}$$

$$p_i = 0, \ \frac{\partial p_i}{\partial t} = 0 \text{ in } \Omega, \ t = 0, \tag{5c}$$

with $\Omega := \Omega_v \cup \Omega_0$, Ω_0 being the volume occupied by the rigid body (see Fig. 2a). In other words, the problem is solved as if the rigid body (in our case the incisors) was absent. After having computed $p_i(\boldsymbol{x}, t)$, the rigid body is inserted again in the computational domain, which leaves one with Ω_v (see Fig. 2b). The diffracted pressure $p_d(\boldsymbol{x}, t)$ is then obtained knowing the value of the incident pressure on the boundary Γ_w of the rigid body, that is to say, solving

$$\frac{1}{c_0^2} \frac{\partial^2 p_s}{\partial t^2} - \nabla^2 p_s = 0 \text{ in } \Omega_v \tag{6a}$$

$$\frac{\partial p_s}{\partial \boldsymbol{n}} = -\frac{\partial p_i}{\partial n} \text{ on } \Gamma_w, \ t > 0 \tag{6b}$$

$$\frac{\partial p_s}{\partial \boldsymbol{n}} = -\frac{1}{c_0} \frac{\partial p_s}{\partial t} \text{ on } \Gamma_\infty, \ t > 0 \tag{6c}$$

$$p_s = 0, \ \frac{\partial p_s}{\partial t} = 0 \text{ in } \Omega_v, \ t = 0. \tag{6d}$$

Note that the summation of problems Eqs. (5) and (6) recovers the original Lighthill analogy in Eq.(1) or the Roger one in Eq. (2), depending on the selected source term in (4).

When applied to the production of /s/, Eq. (5) will provide the incident acoustic contribution $p_i(\boldsymbol{x}, t)$ from the jet flow exiting the mouth to the total sibilant sound, whereas the contribution from the aerodynamic sound diffracted by the incisors will be given by the solution $p_s(\boldsymbol{x}, t)$ to Eq. (6). In this work the factorization into incident and diffracted components has been performed for Lighthill's analogy and only total values for the acoustic pressure are given for that in [29]. However, the strategy could have also been applied to the latter.

C. Numerical strategy

All the partial differential equations in this work have been solved using the method of lines, i.e. the spatial discretization has been carried out with the finite element method (FEM), while finite differences have been adopted for the time discretization. A custom developed software has been used for all computations.

As regards the incompressible Navier-Stokes equations, it is well known that the Galerkin FEM solution suffers from strong instabilities for convection dominated flows and for small time steps at the beginning of evolutionary processes. Moreover, the spatial discrete problem has to satisfy an inf-sup compatibility condition that implies using different interpolation spaces for the incompressible pressure and velocity fields. An efficient way to circumvent all these difficulties is to resort to residual-based stabilized variational multiscale (VMS) methods [see 49, 50]. The unknown variables in the problem weak form become split into large components, resolvable by the finite element mesh, and subgrid scales whose effects onto the large ones have to be modeled. In this work the subscales have been chosen orthogonal to the finite element space and the stabilization parameters have been obtained from a Fourier analysis of the subgrid scale equation [see the orthogonal subgrid scale (OSS) method in 18, 51]. As mentioned in the Introduction, the OSS method acts as an implicit LES model. The stabilized variational Navier-Stokes equations for the problem at hand have been solved using the second order fractional step scheme presented in [52]. A backward differentiation formula of order three (BDF3) has been used for the time discretization.

At each discrete time step, the acoustic source terms in Eq. (4) are computed by post-processing the incompressible pressure and velocity output from the fluid dynamics computation. In the case of Lighthill's analogy, the acoustic waves for the incident and diffracted acoustic pressure, Eqs. (5)-(6), become then solved. The contribution analysis has not been performed for Roger's source term as it would have yielded very similar results to those of Lighthill (see Sec. III B below). Therefore, only Eq. (3) has been solved in this case.

From a computational point of view, the spatial discretization of the wave equation poses no particular problem given that the Laplacian of the acoustic pressure gives rise to a coercive term in the variational form of the problem. Therefore, the main difficulties with the numerical solution of the wave equation arise from the time discretization, which should prevent numerical dissipation as a wave propagates. Given that the focus in this work is on
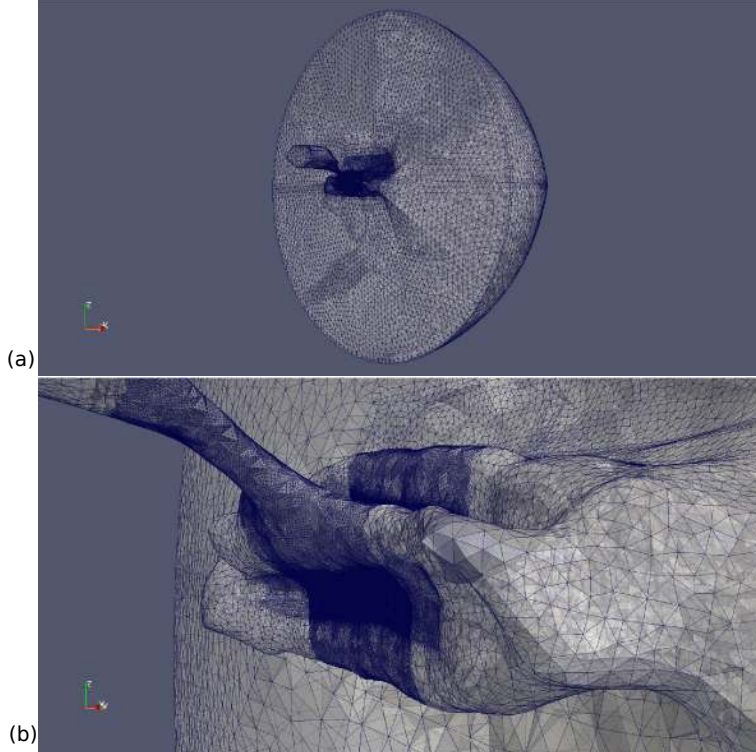
FIG. 3. (a) Meshed computational domain including the vocal tract geometry and the far field (b) Zoom of the refined mesh region. (Color online)

the aerodynamic acoustic pressure at points only a few wavelengths from the mouth, a BDF2 scheme proves accurate enough to approximate the time derivatives in the wave equation and its boundary conditions. Another issue to consider is that of imposing a proper non-reflecting condition at the outer boundary of the computational domain. This often requires the use of a perfectly matched layer (PML) formulation. However, the outwards propagating waves in the present simulations are nearly spherical and impinge in the normal direction to the radiation boundary. Spurious reflections have then been avoided by simply imposing the Sommerfeld condition in [53].

The interested reader is referred to [8] and references therein for a full detailed description of the numerical strategy that has been just outlined.

D. Numerical simulations

To perform the numerical simulations the vocal tract in Fig. 1 has been set in a circular, rigid, flat baffle. A hemispherical domain has been attached to it to allow the flow to

emanate from the mouth and the acoustic waves to propagate outwards (see Fig. 3a).

The following boundary conditions have been applied to solve the incompressible Navier-Stokes equations. A velocity of 2.4 m/s has been prescribed at the inlet section. This has been scaled from the blower in [45] and corresponds to a Reynolds number of Re = 8850, according to the inlet section diameter. Non-slip conditions have been applied to the whole vocal tract and baffle surfaces, while the hemispherical surface has been considered an open boundary, [15]. As regards the acoustic computations, the vocal tract and baffle have been assumed rigid, whereas as mentioned, a non-reflecting Sommerfeld condition has been applied at the hemispherical boundary and at the flow inlet. Since the object of study is a low-Mach flow, no convective/turbulent jets reach these boundaries, for which the sound generation can be considered punctual (seen from the boundaries). This is precisely the assumption that needs to be fulfilled when applying a linear Sommerfeld boundary condition. The following values have been taken for the physical parameters appearing in the equations: an air density of $\rho_0 = 1.2$ kg/m^3, a kinematic viscosity of $\nu = 1.5 \times 10^{-5}$ m^2/s and a sound speed of $c_0 = 343$ m/s.

At low Mach numbers, M, an eddy of characteristic size l essentially radiates sound of wavelength $\lambda \sim \mathcal{O}(l/M)$. Taking into account that the Mach number according to the inlet velocity is $M \sim 0.007$ (though it can locally reach values up to $M \sim 0.23$), and that frequencies up to 12 kHz are to be captured to reproduce the physics of /s/, very fine spatial meshes are required for the simulations. In this work a computational mesh of 45 M linear tetrahedral elements with equal interpolation for all variables has been used (see Fig. 3a and b for a general view and mesh refinement details). The mesh size ranges from $h = 0.025$ mm close to the incisors, where the smallest turbulent flow scales are expected, to $h = 2.5$ mm outside the mouth. The latter guarantees having about twelve nodes per wavelength at 12 kHz ($\lambda \sim 30$ mm).

As explained in the previous section, a total of three equations are solved in the same finite element computational run (four if the acoustic analogy in [29] gets included). Performing such computations with very large size models, as the one in this work, is complex. To that purpose a domain decomposition with an MPI distributed memory scheme has been carried out so as to run the problem at the MareNostrum computer cluster, of the Barcelona Supercomputing Centre (BSC). A period of 10.8 ms with a time step of $\Delta t = 5 \times 10^{-6}$ s has been simulated. This suffices to reach a statistical stationary state. The computational
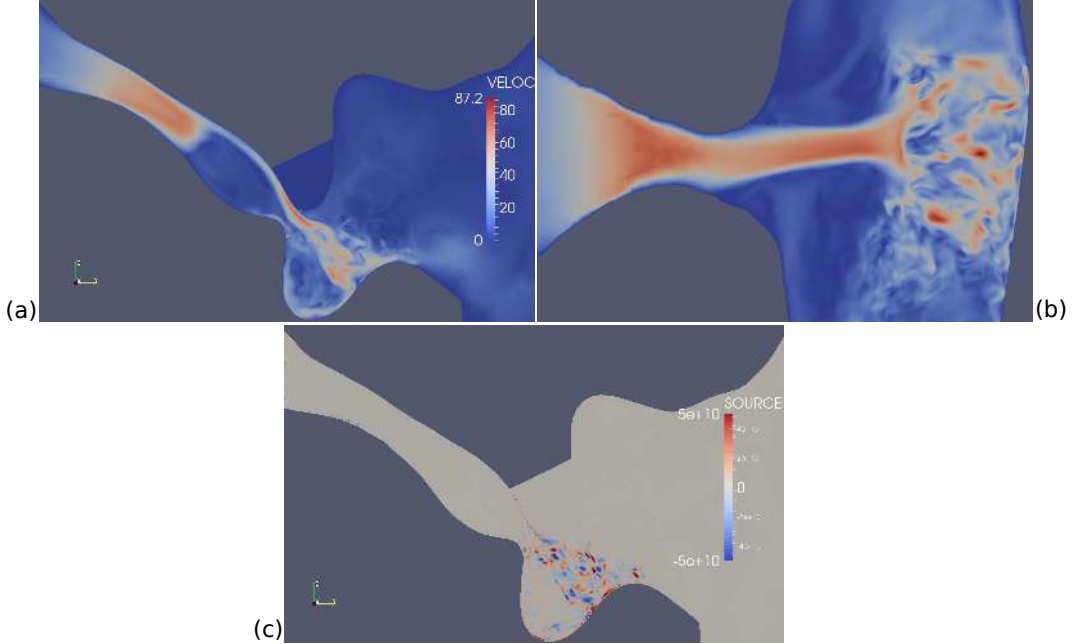
FIG. 4. Snapshot of (a) flow velocity profile in [m/s] on the vertical midplane cut, (b) flow velocity profile on a plane tangent to the tract and (c) Lighthill's acoustic source term at t=0.0108 s in [kg m^{-3}s^{-2}]. (Color online)

run has lasted $\sim$ 30 hours using 256 processors. A Biconjugate Gradients solver with Pilut preconditioner of the Hypre library has been used to solve the FEM algebraic matrix systems, all of them integrated in PETSc.

III.   RESULTS

A.   Flow field and acoustic sources

The qualitative results from the CFD simulation confirm the general theoretical framework describing the mechanisms of /s/ generation, and provide some further insight to it as well. The jet flow is strongly accelerated in the constriction between the tongue blade and the hard palate (see the snapshot in Fig. 4a) giving also rise to a recirculation zone. The flow is greatly accelerated again at the inter-teeth gap reaching local Mach numbers of $M \sim 0.2$. Eddies are shed past the upper incisors and impinge at the lower lips. A strong turbulent flow is generated at the cavity between the lower incisors and lower lips, where most sound sources concentrate. This is shown in Fig. 4c where a snapshot of Lighthill's
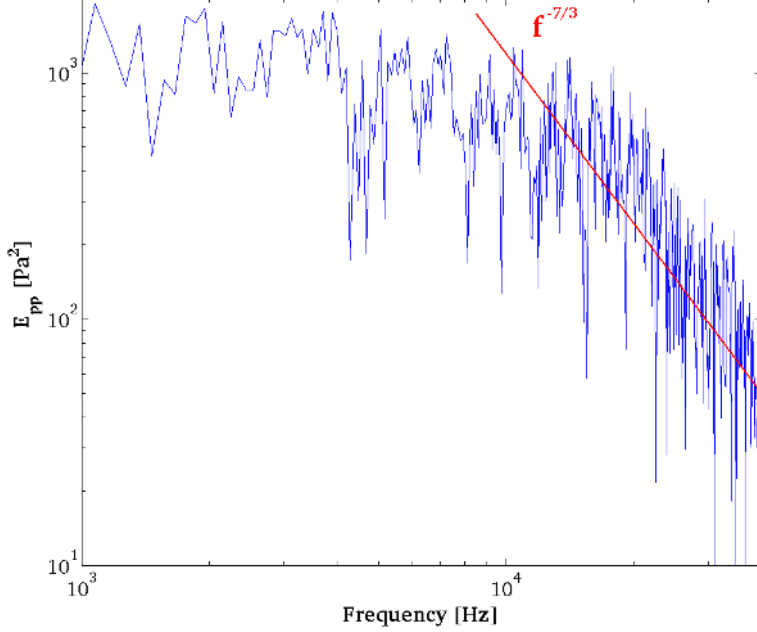
FIG. 5. Spectrum of the incompressible pressure at a near field point showing the right $f^{-7/3}$ dependence at the turbulent inertial subrange. (Color online)

source term, $\rho_0 \left(\nabla \otimes \nabla \right) : \left(\boldsymbol{u}^0 \otimes \boldsymbol{u}^0 \right)$, is presented. The strongest quadrupole sources can be found in the direct path between the edge of the upper incisors, where flow separation takes place, and the top side of the lower lips. The presence of a depression before the constriction in form of a plug which diverts the flow towards the palate, (see Fig. 4a), can be explained with the velocity profile shown at Fig. 4b. It can be observed how the tongue also closes the tract in the transversal direction, forcing the flow to concentrate in a small section of the path before impacting the upper incisors.

To check that the LES has been able to capture all turbulent scales down to the inertial subrange, the incompressible pressure spectrum E_{pp} at an arbitrary point placed just in front of the upper incisors, at coordinates $P1 = (0, 0.0205, -0.012)^\top$, has been plotted in Fig. 5, using a log-log scale. The origin of coordinates is placed at the center of the flat section leading to the realistic vocal tract geometry in Fig. 1. According to Kolmogorov's theory for isotropic turbulence, the energy spectrum at the inertial subrange behaves as $E \sim k^{-5/3}$ while the pressure spectrum as $E_{pp} \sim k^{-7/3}$ (see e.g., [54]). Taylor's hypothesis of frozen turbulence allows one to show the latter also exhibits the same power dependence with frequency, namely $E_{pp} \sim f^{-7/3}$. It is observed in Fig. 5 that the present CFD simulation well recovers the behavior of the pressure spectrum at the inertial subrange, therefore
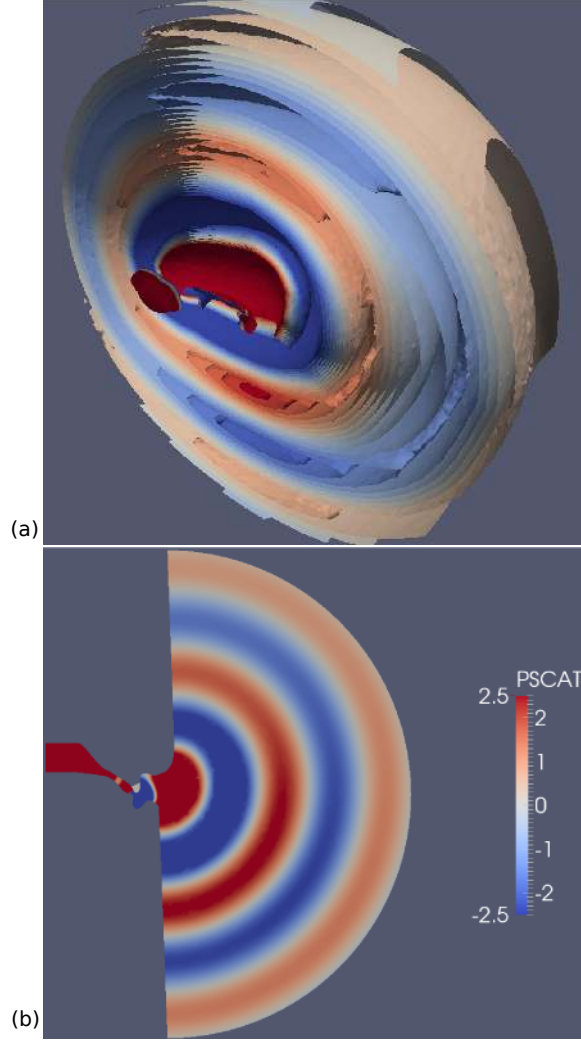
15

FIG. 6. (a) Total acoustic pressure isosurfaces and (b) mid-cut showing diffracted pressure wavefronts. Units in [Pa] (Color online)

showing that the stabilized FEM formulation, combined with the fine computational mesh, corresponds to a large eddy simulation approach.

It is to be noted that quantitative details on the flow dynamics simulation are thought out of the scope of this work, which essentially focus on the generated aerodynamic sound results to be presented in the next subsection.

B. Incident and diffracted sound contributions to the acoustic field

On the one hand, the quadrupole sources depicted in Fig. 4b directly radiate sound which propagates outside the mouth. On the other hand, this sound is partially diffracted by the
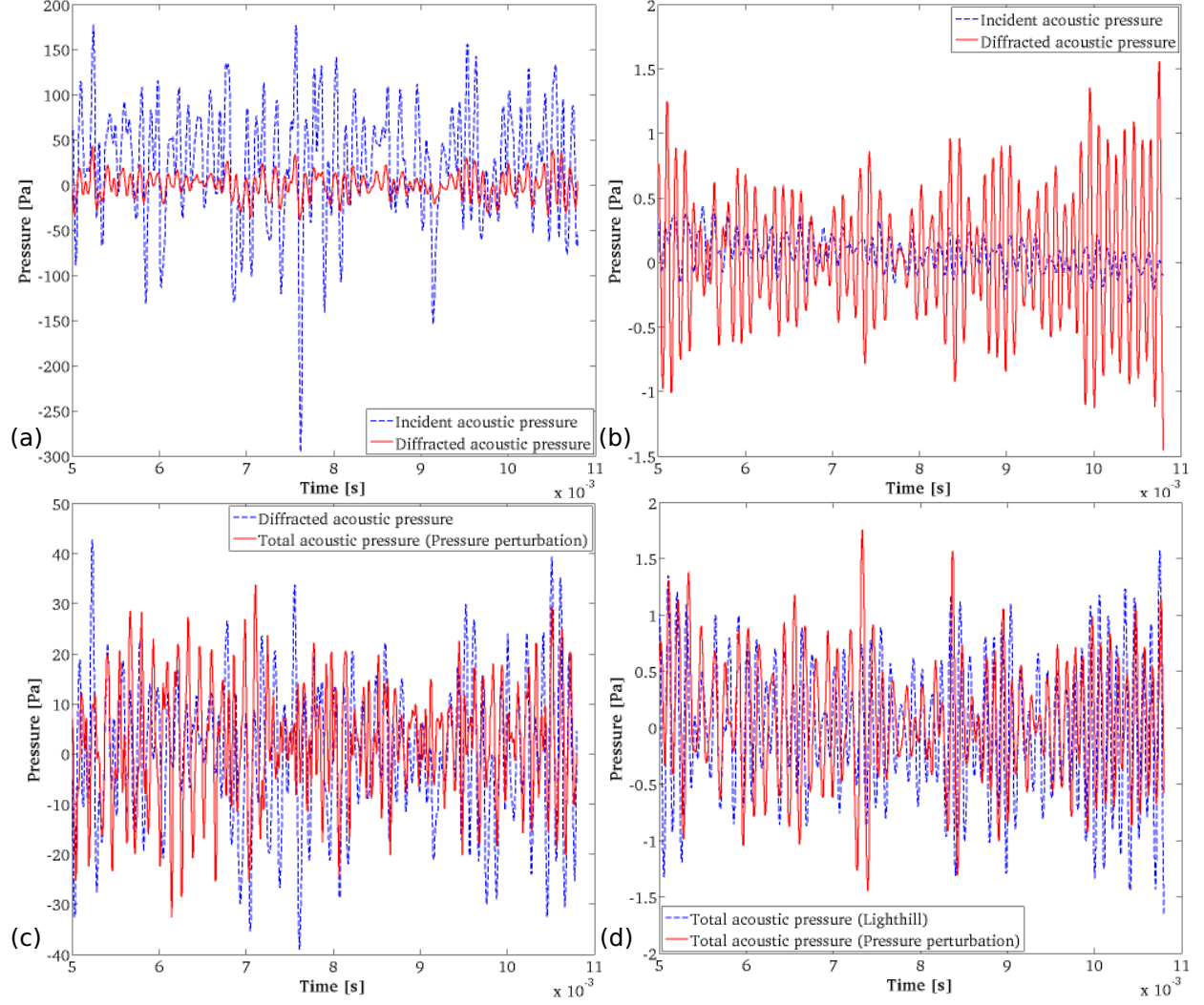
FIG. 7. Time evolution of the acoustic pressure. (a) Incident pseudosound (dashed blue) and diffracted (continuous red) components at the near field point $P1$ from Lighthill's analogy, (b) incident turbulent (dashed blue) and incisor diffracted (continuous red) contributions to the far field point $P5$, (c) Incisors' diffracted contribution using Lighthill's analogy (dashed blue) versus total acoustic pressure (continuous red) using the analogy in [29] at the near field and (d) total acoustic pressure at the far field using Lighthill's analogy (dashed blue) and the analogy in [29] (continuous red). (Color online)

upper incisors and also becomes radiated outwards. As said before, this second mechanism is sought to be the predominant one at the far-field [see e.g., 5]. However, it will be shown that the incident quadrupole radiation cannot be neglected for points in the vicinity of the mouth.

The numerical strategy in Sec. II B has been applied to compute the contributions from the direct quadrupolar sound and the dipolar diffracted one. Before probing more deeply the
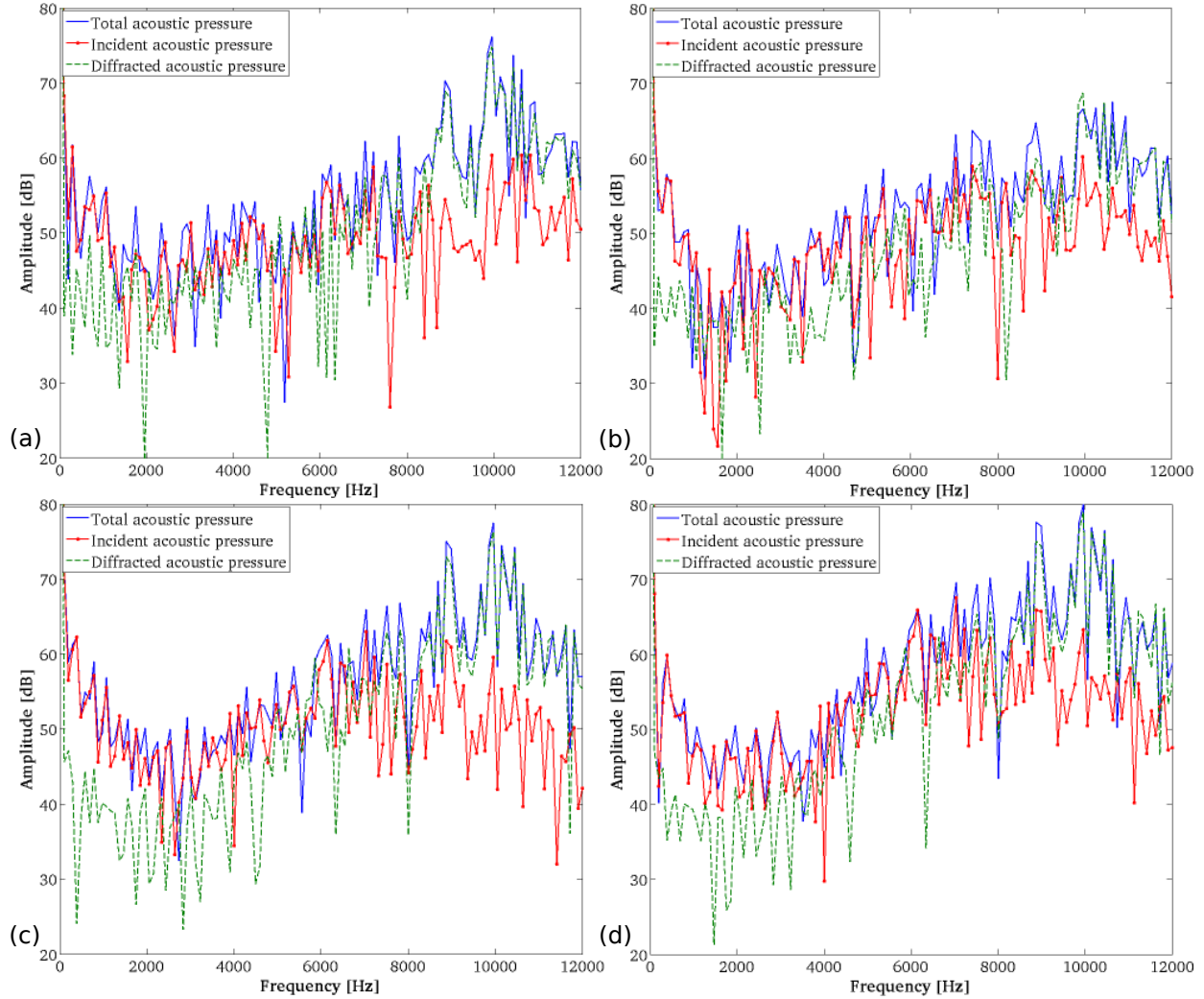
17

FIG. 8. Spectra of the incident, diffracted and total components of the acoustic pressure at the far field. (a) Point $P2$, (b) Point $P3$, (c) Point $P4$, (d) Point $P5$. (Color online)

quantitative results, a snapshot showing the spherical acoustic wavefronts emanating from the mouth is shown in Fig. 6a, whereas a mid-cut showing the propagation of the acoustic waves resulting from the incisors diffraction is presented in Fig. 6b, for illustrative purposes.

Several time history occurrences for the acoustic pressure at two points located at the near field and at the far field are presented in Fig. 7. The first one is point $P1$, already introduced in the previous Sec. III B, whereas the second one is not affected by the flow emanating from the mouth and is placed at $P5 = (0, 0.035, -0.085)^{\top}$, see Figure 1. Figure 7a presents the incident and diffracted contributions to the near field point $P1$ using Lighthill's acoustic analogy. As known, Lighthill's analogy is not valid for points in the source region so the

strong fluctuations from the incident contribution in Fig. 7a (dashed blue line) correspond to pseudosound rather than to acoustic fluctuations. These are one order of magnitude higher than the acoustic contribution from the incisors' diffraction (red continuous line). The contributions for the point at the far field, $P5$ are presented in Fig. 7b. In this case Lighthill's acoustic analogy is perfectly valid to compute the generated aerodynamic acoustic pressure. As observed, at $P5$ the acoustic pressure from the diffracted component is clearly higher than that provided by the direct turbulent flow contribution.

In Fig. 7c, a comparison is presented between the contribution of the incisors' diffraction to the near field point $P1$ (dashed blue line), already plotted in Fig. 7a, and the total acoustic pressure (continuous red line) computed with the acoustic analogy in [29]. Both contributions have the same order of amplitude showing that the analogy in Eq. (3) is capable of filtering the pseudosound and extracting the acoustic component from the pressure fluctuations, at very low Mach numbers. When evaluated at a far field point like $P5$ both, Lighthill's analogy in Eq. (1a) and Eq. (3) should yield almost the same results. This is what is observed in Fig. 7d where the time evolution for the total acoustic pressure at $P5$ using both analogies is plotted. The two curves in the figure show very similar trends in terms of amplitude and phase.

The spectra in dB (ref. 2×10^{-5} Pa) at four points well separated from the flow exiting the mouth, yet close to it, are plotted in Fig. 8. Figs. 8a-d respectively correspond to points $P2 = (-0.075, 0.035, -0.0125)^\top$, $P3 = (0.075, 0.035, -0.0125)^\top$, $P4 = (0, 0.035, 0.06)^\top$ and to $P5$, see Figure 1. The figures contain the total acoustic pressure at these points, together with the contributions from the incident turbulent aerodynamic noise and from the sound diffracted by the incisors. As regards the total acoustic pressure, very similar tendencies can be appreciated in all figures. The spectra first decrease with frequency and exhibit a dip close to 2 kHz; then they increase linearly showing two marked peaks close to 9 kHz and 10 kHz and finally they decrease again with frequency. As regards the contributions, it can be checked that in the range up to 2 kHz the incident turbulent component clearly dominates. The size of the incisors are small compared to the acoustic wavelengths at those frequencies so diffraction is not so important. However, as frequency increases the situation changes and both the incident and diffracted components contribute the same from 2 kHz to ~ 8 kHz, with a slight predominance of the former. Above ~ 8 kHz the turbulent contribution begins to decay and the spectra become mostly justified by the diffracted component. Again, this
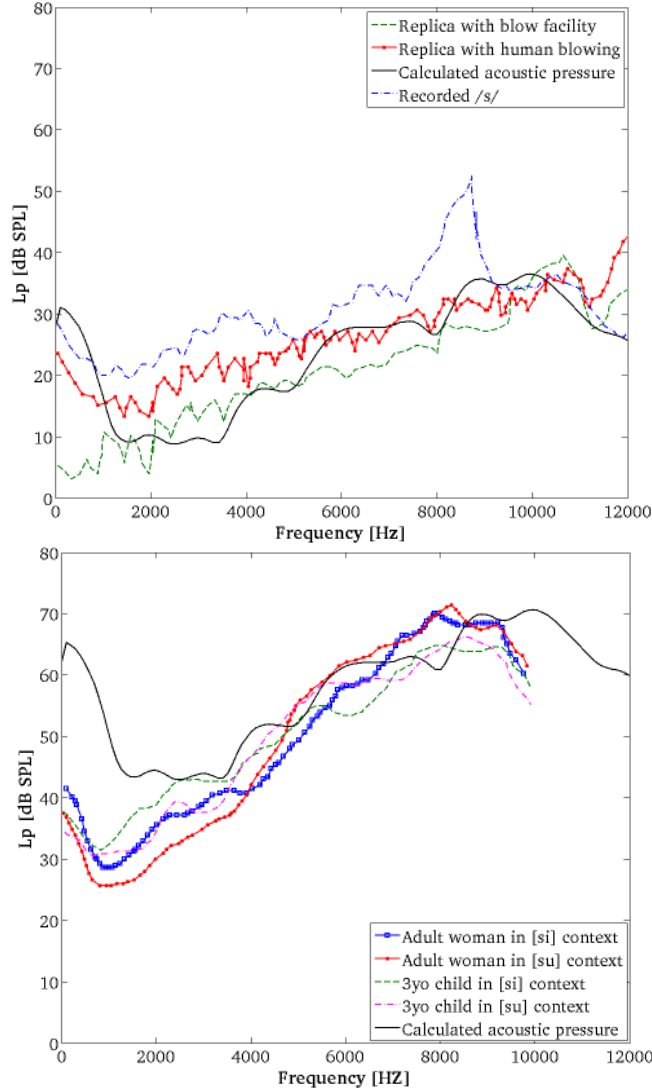
FIG. 9. Comparison of Welch averaged power spectral density levels with (a) the measurements using mechanical replicas in [46] (b) the measurements with subject utterances in [3]. (Color online)

is logical given that for smaller wavelengths the diffraction effects become more important. In addition, more wavelengths are needed to reach the target points and dipolar sources become more effective. For a fixed distance, the conditions of far-field are easier to satisfy at higher frequencies, where the diffracted component is predicted to dominate [see e.g., 5].

C. Comparison with measurements in literature

Given the lack of experimental data with the configuration simulated in the previous section, a comparison with some measurements reported in literature will be next presented.

20

This will serve to somehow validate the general trends of the obtained results.

In particular, some of the data in [46] will be first used for that purpose. In that work a mechanical replica of the geometry in Fig. 1 was built and tested. The experimental setup consisted of a flow facility mechanism that supplied air to an upstream circular duct connected to the vocal tract geometry. No flat baffle was set at the exit of the replica and measurements were taken with a microphone located at 94 cm from the mouth in the yx-plane, and at an angle of 37° in the horizontal xz plane. Reproducing such experiment would have proved prohibitive from a computational point of view. However, a somewhat fair checking of the numerical simulations can be made by comparing the computed spectrum at $P3$ with those in [46] belonging to situation I (recorded speaker), situation II (flow facility with settling chamber plus replica) and situation III (human blowing plus replica), for Re = 8900. For the ease of comparison of the spectral characteristics, the level of the Welch averaged power spectral density [see e.g., 1] at $P3$ has been scaled taking its value at 5 kHz as the average of the values of the measurements at that frequency. The results are presented in Fig. 9a. As observed in the figure, despite all the commented differences the agreement between the computed spectrum and those provided by the replica is pretty good. Unlike the original recording of the speaker, in none of the three cases whistling appears at 9 kHz and the slopes of the spectrum are properly described. These two results are very important because both replica and numerical simulation are based on similar flow conditions, whereas the recording may involve further sources of variation or modulation that have not been taken into account in the modeling. On the other hand, it can be observed that spectral slope, dynamic amplitude and spectral peak are less accurate when comparing with human blowing since these features depend on the imposed volume flow rate, which is less well controlled when air is supplied by human blowing, and due to differences in the inlet turbulence level, which is 0% in the numerical simulation and more than 4% for human blowing, [45],[46].

Comparisons have also been made with the measurements of uttered sibilants in [3]. Recordings with a microphone and a digital spectrograph were provided in that reference for the pronunciation of [s] in the context of phonemes [si] and [su]. Sibilant /s/ was recorded for an adult woman and also for a three year old child. Results are presented in Fig. 9b. Again, the sound pressure level of the Welch averaged power spectral density has been scaled with the average values of the measurements at 5 kHz. As observed in the figure strong

differences can be appreciated at low frequencies, yet the general trends of the spectra are similar. They all exhibit a decay from low frequencies to a dip between $\sim 1-3$ kHz, followed by a strong level increase with frequency up to $\sim 8-9$ kHz, and two peaks whose locations change depending on each realization. The peaks are well separated and can be found approximately at ~ 8.5 kHz and ~ 10 kHz for the spectra at $P3$. They can also be clearly distinguished for the measurements corresponding to phoneme [si], and to a less extent for the adult woman when pronouncing phoneme [su]. Despite considering different speakers (woman and child) and scenarios (the reconstructed geometry portion is obtained for sustained [s] whereas these speech observations are reported for syllables), and taking into account that in [55] is shown that the constriction degree is greater for sustained phonemes than for phonemes in a syllable context, qualitative good agreement is observed for spectral slope and frequency peak.

IV.   CONCLUSIONS

In this work a large-scale numerical simulation of the aeroacoustics of a single example of sibilant fricative [s] has been carried out. Lighthill's acoustic analogy and an analogy that allows filtering pseudosound to some extent at the source region have been implemented. A stabilized finite element method which acts as an implicit large eddy simulation model has been used to solve the incompressible Navier-Stokes equations. The acoustic field has been resolved resorting to a splitting strategy that allows one to obtain the contributions from the incident turbulent sound and the sound diffracted by the upper incisors in a single computational run.

The spectra from the contributions to the total acoustic pressure at points located close to the mouth exit (yet out of the flow wake) reveal a significant different behavior depending on the frequency range. At the lowest side of the spectrum, the acoustic pressure level decreases and the incident turbulent sound directly emanating from eddies in the cavity between incisors and lips dominates. This is the case up to ~ 2 kHz. From ~ 2 kHz to $\sim 8-9$ kHz, the level strongly increases and the contributions from both the sound diffracted by the upper incisors and from turbulence are very similar. At higher frequencies the diffracted sound becomes dominant.

Finally, one should bear in mind that the results reported in this work correspond to a

single vocal tract geometry extracted from a subject while uttering a particular realization of [s]. Therefore, care should be taken not to give general validity to the conclusions. However, comparisons with measurements in literature on mechanical replicas and subject recordings seem to validate the main trends of the obtained results.

ACKNOWLEDGMENTS

[1] Jesus, L.M.T., Shadle, C.H. (2002). A parametric study of the spectral characteristics of European Portuguese fricatives, J. Phonetics **30**, **3**, 437–464.

[2] Narayanan, S.S., Alwan, A.A., Haker, K. (1995). An articulatory study of fricative consonants using magnetic resonance imaging, J. Acoust. Soc. Am. **98**, **3**, 1325–1347.

[3] Nittrouer, S., Studdert-Kennedy, M., McGowan, R.S. (1989). The Emergence of Phonetic SegmentsEvidence from the Spectral Structure of Fricative-Vowel Syllables Spoken by Children and Adults, JSLHR **32**, **1**, 120–132.

[4] Gracco, V.L., Lofqvist, A. (1994). Speech motor coordination and control: evidence from lip, jaw, and laryngeal movements, J. Neuroscience **14**, **11**, 6585–6597.

[5] Howe, M.S., McGowan, R.S. (2005). Aeroacoustics of [s], Proc. R. Soc. A. **461**, **2056**, 1005–1028.

[6] Howe, M.S. (1998). Acoustics of fluid-structure interactions, Cambridge University Press.

[7] Yoshinaga, T., Koike, N., Nozaki, K., Wada, S. (2015). Study on production mechanisms of sibilants using simplified vocal tract model, INTER-NOISE and NOISE-CON Congress and Conference Proceedings **250**, **1**, 5662–5669.

[8] Guasch, O., Pont, A., Baiges, J., Codina, R. (2016). Concurrent finite element simulation of quadrupolar and dipolar flow noise in low Mach number aeroacoustics, Comput. Fluids **133**, 129–139.

[9] Bailly, C., Bogey, C., Gloerfelt, X. (2005). Some useful hybrid approaches for predicting aerodynamic noise, C. R. Mec. **333**, **9**, 666–675.

[10] Williams, J.E.F., Hawkings, D.L. (1969). Sound generation by turbulence and surfaces in arbitrary motion, Phil. Trans. Roy. Soc. A. **264**, **1151**, 321–342.

[11] Curle, N. (1955). The influence of solid boundaries upon aerodynamic sound, Proc. R. Soc. Lond. A. **231**, **1187**, 505–514.

[12] Martínez-Lera, P., Schram, C., Bériot, H., Hallez, R. (2014). An approach to aerodynamic sound prediction based on incompressible-flow pressure, J. Sound Vib. **333**, **1**, 132–143.

[13] Van Hirtum, A., Grandchamp, X., Cisonni, J., Nozaki, K., Bailliet, H. (2012). Numerical and experimental exploration of flow through a teeth-shaped nozzle, Adv. Appl. Fluid Mech. **11**, 87–117.

[14] Van Hirtum, A., Grandchamp, X., Pelorson, X., Nozaki, K., Shimojo, S. (2010). LES and" in Vitro" Experimental Validation of Flow around a Teeth-Shaped Obstacle, Int. J. Appl. Mech. **2**, **2**, 265–279.

[15] Cisonni, J., Nozaki, K., Van Hirtum, A., Grandchamp, X., Wada, S. (2013). Numerical simu-

lation of the influence of the orifice aperture on the flow around a teeth-shaped obstacle, Fluid Dyn. Res. **45**, **2**.

[16] Cisonni, J., Nozaki, K., Van Hirtum, A., Wada, S. (2011). A Parameterized Geometric Model of the Oral Tract for Aero acoustic Simulation of Fricatives, IJIEE **1**, **3**, 223.

[17] Nozaki, K. (2010). Numerical simulation of sibilant [s] using the real geometry of a human vocal tract, High Performance Computing on Vector Systems 137–148.

[18] Codina, R., Principe, J., Guasch, O., Badia, S. (2007). Time dependent subscales in the stabilized finite element approximation of incompressible flow problems, Comput. Methods Appl. Mech. Engrg. **196**, **21**, 2413–2430.

[19] Gravemeier, V. (2006). The variational multiscale method for laminar and turbulent flow, Arch. Computat. Methods Eng. **13**, **2**, 249–324.

[20] Sagaut, P. (2006). Large eddy simulation for incompressible flows: an introduction, 1–290, Springer Science & Business Media.

[21] Colomés, O., Badia, S., Codina, R., Principe, J. (2015). Assessment of variational multiscale models for the large eddy simulation of turbulent incompressible flows, Comput. Methods Appl. Mech. Engrg. **285**, 32–63.

[22] Principe, J., Codina, R., Henke, F. (2010). The dissipative structure of variational multiscale methods for incompressible flows, Comput. Methods Appl. Mech. Engrg. **199**, **13**, 791–801.

[23] Massarotti, N., Nithiarasu, P., Codina, R., Principe, J., Ávila, M. (2010). Finite element approximation of turbulent thermally coupled incompressible flows with numerical sub-grid scale modelling, Int. J. Num. Meth. Heat & Fluid Flow **20**, **5**, 492–516.

[24] Guasch, O. and Codina, R. (2013). Statistical behavior of the orthogonal subgrid scale stabilization terms in the finite element large eddy simulation of turbulent flows, Comput. Methods Appl. Mech. Engrg. **261**, 154–166.

[25] Bailly, C., Bogey, C. (2004). Contributions of computational aeroacoustics to jet noise research and prediction, Int. J. Comput. Fluid Dyn. **18**, **6**, 481–491.

[26] Ewert, R., Schröder, W. (2003). Acoustic perturbation equations based on flow decomposition via source filtering, J. Comput. Phys. **188**, **2**, 365–398.

[27] Hueppe, A., Kaltenbacher, M. (2012). Spectral finite elements for computational aeroacoustics using acoustic perturbation equations, J. Comput. Acoust. **20**, **2**.

[28] Guasch, O., Sánchez-Martín, P., Pont, A., Baiges, J., Codina, R. (2016). Residual-based

stabilization of the finite element approximation to the acoustic perturbation equations for low Mach number aeroacoustics, Int. J. Numer. Meth. Fluids. **82**, **12**, 839–857.

[29] Roger, M. (2006). Aeroacoustics: Some theoretical background. The acoustic analogy, Computational Aeroacoustics.

[30] Lighthill, M.J. (1952). On sound generated aerodynamically. I. General theory, Proc. R. Soc. Lond. A **211**, **1107**, 564–587.

[31] Crighton, D.G., Dowling, A.P., Ffowcs-Williams, J.E., Heckl, M., Leppington, F.G. (1996). Modern methods in analytical acoustics, Journal of Fluid Mechanics **318**, 410–412.

[32] Arnela, M., Guasch, O. (2013). Finite element computation of elliptical vocal tract impedances using the two-microphone transfer function method, J. Acoust. Soc. Am. **133**, **6**, 4197–4209.

[33] Speed, M., Murphy, D.T., Howard, D.M. (2013). Three-Dimensional digital waveguide mesh simulation of cylindrical vocal tract analogs, IEEE Trans. Audio Speech Lang. Process. **21**, **2**, 449–455.

[34] Vampola, T., Horáček, J., Švec, J.G. (2008). FE modeling of human vocal tract acoustics. Part I: Production of Czech vowels, Acta Acust. united Ac. **94**, **3**, 433–447.

[35] Vampola, T., Horáček, J., Švec, J.G. (2015). Modeling the influence of piriform sinuses and valleculae on the vocal tract resonances and antiresonances, Acta Acust. united Ac. **101**, **3**, 594–602.

[36] Arnela, M., Dabbaghchian, S., Blandin, R., Guasch, O., Engwall, O., Van Hirtum, A., Pelorson, X. (2016). Influence of vocal tract geometry simplifications on the numerical simulation of vowel sounds, J. Acoust. Soc. Am. **140**, **3**, 1707–1718.

[37] Takemoto, H., Mokhtari, P., Kitamura, T. (2010). Acoustic analysis of the vocal tract during vowel production by finite-difference time-domain method, J. Acoust. Soc. Am. **128**, **6**, 3724–3738.

[38] Arnela, M., Blandin, R., Dabbaghchian, S., Guasch, O., Alías, F., Pelorson, X., Van Hirtum, A., Engwall, O. (2016). Influence of lips on the production of vowels based on finite element simulations and experiments, J. Acoust. Soc. Am. **139**, **5**, 2852–2859.

[39] Arnela, M., Guasch, O., Alías, F. (2013). Effects of head geometry simplifications on acoustic radiation of vowel sounds based on time-domain finite-element simulations, J. Acoust. Soc. Am. **134**, **4**, 2946–2954.

[40] Blandin, R., Arnela, M., Laboissière, R., Pelorson, X., Guasch, O., Van Hirtum, A., Laval, X.

(2015). Effects of higher order propagation modes in vocal tract like geometries, J. Acoust. Soc. Am. **137**, **2**, 832–843.

[41] Blandin, R., Van Hirtum, A., Pelorson, X., Laboissière, R. (2016). Influence of Higher Order Acoustical Propagation Modes on Variable Section Waveguide Directivity: Application to Vowel [α], Acta Acust. united Ac. **102**, **5**, 918–929.

[42] Guasch, O., Arnela, M. Codina, R., Espinoza, H. (2016). A stabilized finite element method for the mixed wave equation in an ALE framework with application to diphthong production, Acta Acust. united Ac. **102**, **1**, 94–106.

[43] Krane, M.H. (2005). Aeroacoustic production of low-frequency unvoiced speech sounds, J. Acoust. Soc. Am. **118**, **1**, 410–427.

[44] Anderson, P., Green, S., Fels, S. (2009). Modeling fluid flow in the airway using CFD with a focus on fricative acoustics, International Workshop on Dynamic Modeling of the Oral, Pharyngeal and Laryngeal Complex for Biomedical Applications. **Proc. 1st**, 146–154.

[45] Van Hirtum, A., Fujiso, Y., Nozaki, K. (2014). The role of initial flow conditions for sibilant fricative production, J. Acoust. Soc. Am. **136**, **6**, 2922–2925.

[46] Fujiso, Y., Nozaki, K., Van Hirtum, A. (2015). Towards sibilant physical speech screening using oral tract volume reconstruction: Some preliminary observations, Appl. Acoust. **96**, 101–107.

[47] Guasch, O. and Codina, R. (2009). Computational aeroacoustics of viscous low speed flows using subgrid scale finite element methods, J. Comput. Acoust. **17**, **3**, 309–330.

[48] Gloerfelt, X., Pérot, F., Bailly, C., Juvé, D. (2005). Flow-induced cylinder noise formulated as a diffraction problem for low Mach numbers, J. Sound Vib. **287**, **1**, 129–151.

[49] Hughes, T.J.R. (1995). Multiscale phenomena: Green's functions, the Dirichlet-to-Neumann formulation, subgrid scale models, bubbles and the origins of stabilized methods, Comput. Methods Appl. Mech. Engrg. **127**, **1**, 387–401.

[50] Hughes, T.J.R., Feijóo, G.R., Mazzei, L., Quincy, J.B. (1998). The variational multiscale method a paradigm for computational mechanics, Comput. Methods Appl. Mech. Engrg. **166**, **1**, 3–24.

[51] Codina, R. (2002). Stabilized finite element approximation of transient incompressible flows using orthogonal subscales, Comput. Methods Appl. Mech. Engrg. **191**, **39**, 4295–4321.

[52] Codina, R., Badia, S. (2006). On some pressure segregation methods of fractional-step type

for the finite element approximation of incompressible flow problems, Comput. Methods Appl. Mech. Engrg. **195**, **23**, 2900–2918.

[53] Espinoza, H., Codina, R., Badia, S. (2014). A Sommerfeld non-reflecting boundary condition for the wave equation in mixed form, Comput. Methods Appl. Mech. Engrg. **276**, 122–148.

[54] Pope, S.B. (2000). Turbulent Flows, Cambridge University Press.

[55] Fujiso, Y., Nozaki, K., Van Hirtum, A. (2015). Estimation of minimum oral tract constriction area in sibilant fricatives from aerodynamic data, JASA **138**, **1**, EL20–EL25.

Fig. 1. 3D realistic vocal tract geometry for [s] with upper incisors highlighted in green. Measuring points P4 and P5 are placed at the far-field. (Color online).

Fig. 2. Domains for computing (a) the incident acoustic pressure and (b) the diffracted acoustic pressure in the proposed splitting strategy for aeroacoustics. (Color online).

Fig. 3. (a) Meshed computational domain including the vocal tract geometry and the far field (b) Zoom of the refined mesh region. (Color online).

Fig. 4. Snapshot of (a) flow velocity profile in [m/s] on the vertical midplane cut, (b) flow velocity profile on a plane tangent to the tract and (c) Lighthill's acoustic source term at t=0.0108 s in [kg m^{-3}s^{-2}]. (Color online).

Fig. 5. Spectrum of the incompressible pressure at a near field point showing the right $f^{-7/3}$ dependence at the turbulent inertial subrange.

Fig. 6. (a) Total acoustic pressure isosurfaces and (b) mid-cut showing diffracted pressure wavefronts. Units in [Pa] (Color online).

Fig. 7. Time evolution of the acoustic pressure. (a) Incident pseudosound (dashed blue) and diffracted (continuous red) components at the near field point $P1$ from Lighthill's analogy, (b) incident turbulent (dashed blue) and incisor diffracted (continuous red) contributions to the far field point $P5$, (c) Incisors' diffracted contribution using Lighthill's analogy (dashed blue) versus total acoustic pressure (continuous red) using the analogy in [29] at the near field and (d) total acoustic pressure at the far field using Lighthill's analogy (dashed blue) and the analogy in [29] (continuous red). (Color online). (Color online).

Fig. 8. Spectra of the incident, diffracted and total components of the acoustic pressure at the far field. (a) Point $P2$, (b) Point $P3$, (c) Point $P4$, (d) Point $P5$. (Color online).

Fig. 9. Comparison of Welch averaged power spectral density levels with (a) the measurements using mechanical replicas in [46] (b) the measurements with subject utterances in [3].